

# Additive texturing of metallic surfaces for wetting control

[Additive Manufacturing 37 \(2021\) 101631](#)

S. Mekhiel <sup>a,b</sup>, Philip Koshy <sup>a</sup>, M. A. Elbestawi <sup>a</sup>

<sup>a</sup>Department of Mechanical Engineering, McMaster University, Hamilton, Canada.

<sup>b</sup>Machine Design and Production Department, Military Technical College, Cairo, Egypt.

## Abstract

Additive Manufacturing (AM) has enabled the realization of custom products with intricate geometric features that are either too complex or even intractable for subtractive manufacturing processes. On the other hand, owing to their relatively poor roughness, functional surfaces generated in AM have to be often finish machined. This research explored the prospect of turning this limitation around by pursuing a novel concept of Additive Texturing (AT) wherein the topography of an AM part is tailored in-process to entail textures that further enhance the functionality of an AM product. In this context, the limits of the selective laser melting process in printing metallic surface microfeatures were investigated as a precursor to realizing texture patterns comprising pillars, channels, and re-entrant structures. Following on from this, the efficacy of such textures in controlling the wetting behaviour of stainless steel AM surfaces was examined. The notion of AT is demonstrated in terms of its capability to generate hydrophobic AM surfaces with water contact angles exceeding 140°.

*Keywords:* Additive Manufacturing, Hydrophobicity, Selective Laser Melting, Surface Texturing, Wettability.

## 1. Introduction

Additive Manufacturing (AM) technologies have emerged to occupy a niche domain in the realm of manufacturing processes on account of the design freedom they offer to enhance component functionality. This is particularly true in terms of the capability of AM to realize features of a

complex geometry that are either expensive or impossible to manufacture using conventional subtractive manufacturing processes, due to restrictions arising from tooling access. Additionally, attributes that render AM to be appealing are the significant decrease in the lead time from design to product realization, advantages accruing from a reduction in the number of parts, and the cost and time savings associated with machine set-up, tooling and assembly [1].

The work presented in this paper seeks to further expand the application envelope and process capability of AM processes by introducing the novel notion of “Additive Texturing” (AT). This refers to the adaptation of AM towards engineering the topography of a printed surface towards realizing functional attributes. This represents a significant value addition as it enables AM parts to comprise a surface functionality through in-place printing of textured surfaces with designed surface features, without having to invoke additional secondary processes. The present work will specifically refer to selective laser melting (SLM) of metallic components with a continuous laser, and demonstrate the concept by printing and testing surfaces that have been designed to possess controlled wettability. Currently, there appears to have been only one such SLM-related texturing work: the fabrication of microcavities and microfins, which by virtue of being active bubble nucleation sites have been shown to be effective in enhancing the heat transfer coefficient and critical heat flux in pool boiling [2].

A significant extent of AM research has focused on microstructure in the component bulk, and the characterization of material-specific mechanical properties of components such as relative density, strength, microhardness and residual stresses [1]. This has led to the process–structure–property paradigm that is considered the core of AM research and development. Investigations on surfaces generated in AM on the other hand have thus far not been as widely investigated. Although surface features are indeed signatures of complex multi-physical phenomena underlying the AM process, in several instances AM surfaces have been characterized only towards assessing the capability of the AM technology at hand [3]. Currently, metrology of AM surface textures is likewise somewhat rudimentary, with measurements largely limited to two-dimensional stylus measurements [3]. This is perhaps not entirely surprising given that in most applications the built surface would have to be post-processed using machining to obtain a surface quality consistent with functional requirements. The present work strives to flip the surface quality limitation of AM around into engineering the topography of a printed surface, so as to realize surfaces with defined features to impart controlled wettability.

Bio-inspired texturing of functional surfaces has of late garnered the attention of researchers resulting in intriguing applications [4]. Examples include dimpled features that can trap lubricants and wear debris to enhance tribological response, features that can facilitate osseointegration of biomedical implants, and generation of features that can manipulate attributes like coating adhesion, fluid drag, and surface traction. The present work focuses on surface wetting as alluded to previously, and specifically refers to water-repellant (hydrophobic) surfaces inspired by biological surfaces such as lotus leaves. Such surfaces may be generated using processes like sol-gel processing, lithography and electrospinning, however, they pertain to soft materials like polymers that lack mechanical durability. For fabricating robust metallic surfaces, laser micromachining [5] and electrical discharge machining (EDM) [6] have been effective. Given the microscale of the textures generated in these processes, the substrate would need to be polished for such textural features to be functionally effective [7]. Considering that the high surface roughness inherent to additively manufactured surfaces would inevitably mask the microfeatures, the as-built surfaces would need to be finish machined and polished prior to texturing. This represents additional infrastructure and multiple process steps that significantly add to the processing time and cost. To this end, the objective of the present work has been to generate metallic hydrophobic surfaces in-process and in a single step directly using SLM with no requirements for post-processing.

Considering that standard texture features are typically on the microscale, a knowledge of the minimum feature size and spacing possible in SLM is a precursor to texturing investigations. A number of designs to benchmark the performance of AM processes and machines in terms of geometrical and dimensional accuracy, repeatability, and minimum feature size are available in the literature, a comprehensive review of which can be found in [8]. Feature sizes considered in these works are on the order of mm which does not quite fall into the domain of texturing. A minimum feature size of 0.25 mm has been considered in an artifact intended for standardization [9]. A test part to characterize micro AM is reported in [10], however, this relates to digital light processing using polymer resins. Fine features obtainable in SLM are material dependent and are limited by the extent of the heat-affected zone, the positioning accuracy of the laser system, and the beam width compensation [9]. Accordingly, in the first phase of the present work, test coupons were designed and printed based on the guidelines offered in [8] to identify limiting feature attributes that are specific to the material, machine and processing parameters adopted.

Following test artifact investigations, this work investigated the surface roughness of the as-built surfaces under various process parameters, and their wettability was assessed in terms of the static contact angle (CA) with water as the working fluid. Single tracks were printed thereafter to identify the minimum achievable line width. This was followed by investigations on top and side surfaces (normal and parallel to the build direction) printed with pillar, channel and re-entrant pattern arrays of various dimensions to characterize the corresponding wettability, which provided the proof-of-concept of generating hydrophobic surfaces with CA exceeding 140°.

## **2. Experimental**

### **2.1. Material and process parameters**

The feedstock was a gas atomized AISI 316L stainless steel powder of 15–45  $\mu\text{m}$  particle size. Samples were built using an SLM machine (EOS M280) with a 400 W continuous ytterbium fiber laser, in a nitrogen atmosphere. The layer thickness and stripe width were maintained constant at 0.04 mm and 100  $\mu\text{m}$ , respectively. Samples were positioned on the build plate within the stripe width to avoid stripe overlap. The effect of process parameters was interpreted in terms of the volumetric ( $E_V$ ) and linear ( $E_L$ ) energy densities, respectively obtained as  $(P/vht)$  and  $(P/vt)$ , where  $P$  is the laser power,  $v$  is the scanning speed,  $t$  is the layer thickness and  $h$  is the hatch spacing.

### **2.2. Artifacts for limiting feature dimensions**

Three custom coupon designs were used to assess the limiting dimensions in SLM. The first coupon comprised periodic protruding trapezoidal features wherein the parallel sides decreased linearly from 0.6 mm to 0.01 mm over a length of 45 mm, to continuously assess the minimum printable feature width. The space between the protruding features corresponds to sunk trapezoidal features (Fig. 1a). The coupon had twelve such trapezoids of depths ranging from one to twelve layer thickness, to detect any interaction between the limiting feature width and depth.

The second coupon referred to the minimum spacing between protruding and sunk features of 0.4 mm width and was of a geometry shown in Fig. 1b. The spacing was altered from 0.5 mm to 0.1 mm in increments of 0.1 mm, and from 0.1 and 0.01 mm in increments of 0.01 mm. The

depth of all features was held constant at 0.4 mm. Both coupons were printed using two sets of process parameters (Table 1), which were previously identified to correspond to the maximum density and strength for the same material and machine [11].

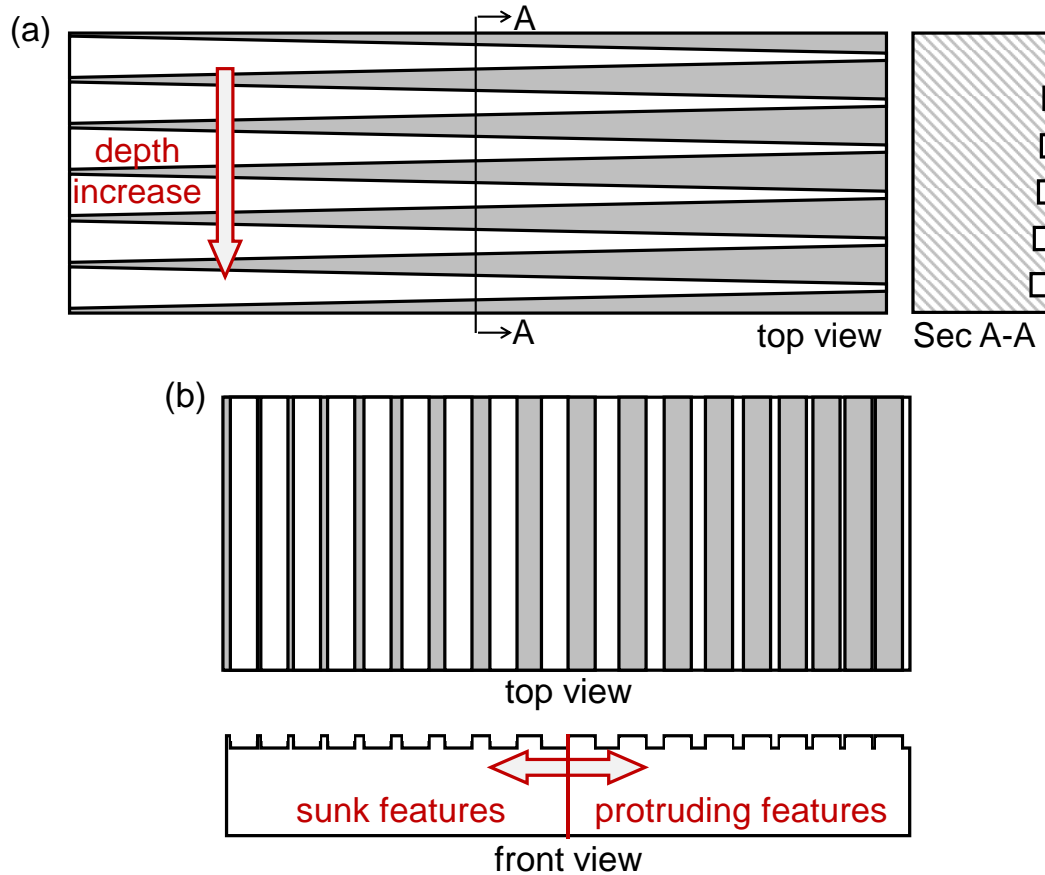


Fig. 1. Schematic of coupons to assess limiting feature geometry in terms of: (a) width, and (b) spacing.

Table 1. Process parameters for coupon builds.

Process parameter	$P$ (W)	$v$ (mm/s)	$h$ (mm)	$t$ (mm)	$E_v$ (J/mm <sup>3</sup> )	Remarks
Set 1	250	800	0.08	0.04	97.7	Maximum density
Set 2	300	1000	0.12	0.04	62.5	Maximum strength

The third coupon pertained to the limiting width of single tracks, which were printed in a single pass under different combinations of scanning speed (ten levels, from 200 mm/s to 2000 mm/s) and laser power (eight levels, from 50 W to 370 W). The tracks were of 3 mm length and were printed in a direction perpendicular to the scanning direction of the layer on which they were printed.

### 2.3. Artifacts for defined texture features

Square pillars (Fig. 2a) and rectangular channels (Fig. 2b) were built on top of 10 mm x 10 mm base samples. The dimensions of these features (Table 2) were based on information obtained from building coupons meant to determine minimum feature size (Sec.2.2). Pillars were built using bi-directional scanning with a hatch spacing of 0.1 mm, using a laser power and scanning speed of 300 W and 800 mm/s, respectively, with the coupon edges oriented parallel to the scanning axes. Widening the hatch spacing values (0.2 mm to 0.5 mm), the second pattern was fabricated using the same process parameters, to realize the geometry of the individual channels.

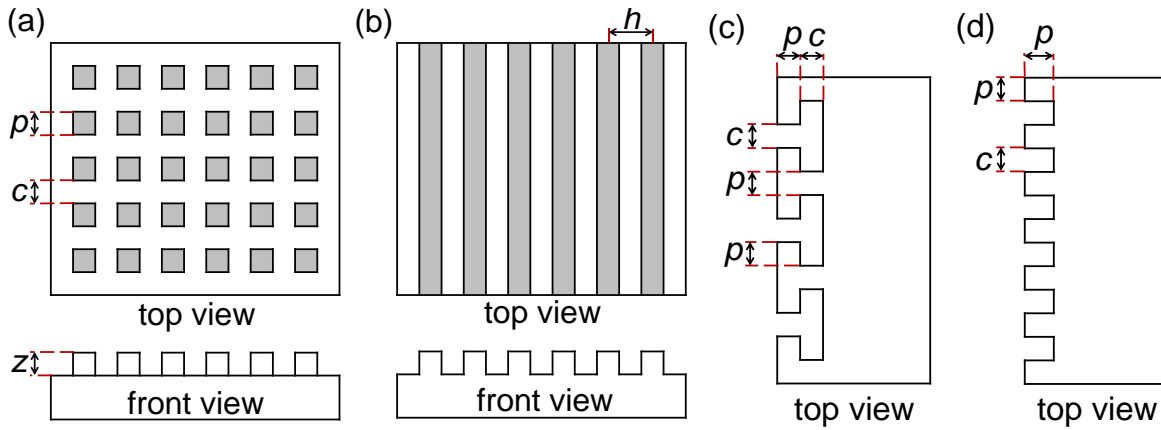


Fig. 2. Texturing patterns on top surface: (a) pillars, (b) channels; and on sidewall: (c) re-entrants, and (d) channels.

In addition to textures on the top surface, re-entrant features (Fig. 2c) and channels (Fig. 2d) were built on the side walls (parallel to the build direction) using the same process parameters as above, on samples of a section of 5 mm x10 mm and a height of 7 mm. The dimensions of these features were the same as that of the top surface cavities and pillars (Table 2).

Table 2. Dimensions (in mm) for designed texture features on the top surface.

Square pillars	$c$	0.15, 0.20, 0.25
	$p$	0.10, 0.15
	$z$	0.04, 0.08, 0.12, 0.16
Rectangular channels	$h$	0.20, 0.25, 0.30, 0.35, 0.40, 0.45, 0.50
	$z$	0.04, 0.08, 0.12, 0.16, 0.20

## 2.4. Characterization

Built coupons were examined using optical and scanning electron microscopy. Roughness was measured with a stylus profilometer in terms of the  $Ra$  parameter, using 5 measurements on each sample. The static CA was measured optically with 5  $\mu\text{L}$  distilled water droplets, using six measurements across different sample locations. Samples were elevated gradually to facilitate water droplets being picked up by the surface from the dosing syringe, rather than drop on the surface and thereby introduce measurement errors [12]. The estimation of CA entailed the Axisymmetric Drop Shape Analysis (ADSA) fitting method [13]. In light of probable temporal evolution of CA [6], measurements were undertaken at least three weeks after printing.

## 3. Results and Discussion

### 3.1. Roughness and contact angle of as-built surfaces

In view of the objective of the present work in exploring the role of additive texturing in controlling the wettability of metallic surfaces, it was imperative to first characterize and benchmark the roughness and CA of as-built surfaces for a range of SLM parameters and examine any correlations between the roughness and CA of such surfaces. To this end, top and side surfaces were investigated for a range of process parameters: power 200–300 W, scanning speed 600–1000 mm/s and hatch spacing 0.08–0.12 mm [11], and their effects were collectively interpreted in terms of the volumetric energy density  $E_v$  (Fig. 3a).

For about a three-fold change in  $E_v$  (41.2–157 J/mm<sup>3</sup>) the  $Ra$  roughness (measured perpendicular to the scanning direction) of top surfaces manifested roughly a five-fold non-linear decrease (14.5–3.1  $\mu\text{m}$ ). This trend aligns with that reported in [14] and could be attributed to the combination of high laser power, low scanning speed and low hatch spacing jointly promoting a more uniform spatial distribution of a larger pool of molten material [15].

For such a large variation in  $Ra$  roughness, the measurement of CA indicated a variation of only 20° (in the range of 80°–100°) with no systematic trends. This is similar to the observation in [6], which dealt with the application of EDM in fabricating hydrophobic surfaces, that the CA varied over a similar range ( $\sim 20^\circ$ ) for a five-fold increase in the  $Ra$  roughness. For a given surface, the

CA values also exhibited significant variability (mean standard deviation of  $5^\circ$ ) signifying the metastable nature of the states that the water droplet can exist in. Fig. 3a provides a visual representation of the water droplets on surfaces corresponding to extremes within the range of roughness values investigated, with CA of  $90^\circ$  and  $93^\circ$ .

Given that the equilibrium CA of a polished surface of 316L stainless steel is reportedly  $75^\circ$  [16], the increase in CA ( $80^\circ$ – $100^\circ$ ) obtained with SLM may be attributed to changes in surface topography in line with Wenzel/Cassie-Baxter models [12], and possible changes to the chemistry of these surfaces over time [17]. The increase in CA for as-built surfaces is rather modest over such a relatively large range of roughness. This implies that a further increase in CA would likely have to be obtained through defined textures that are realized in-process during SLM, which is the fundamental tenet of this paper.

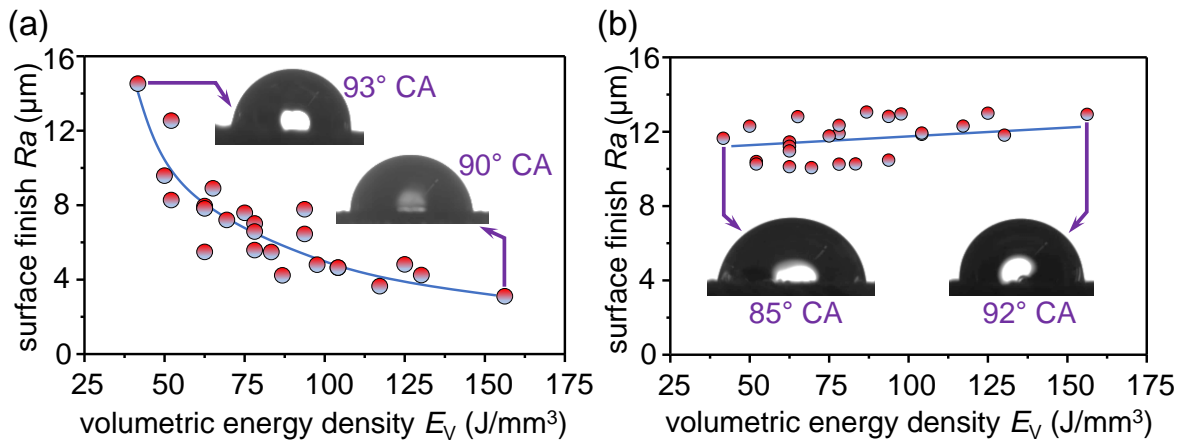


Fig. 3. The roughness of: (a) top, and (b) side surfaces; insets show droplet shapes and CA for extreme values.

In contrast to the top surfaces that displayed a wide range in roughness and a declining trend with  $E_v$  (Fig. 3a), the roughness of side surfaces (Fig. 3b) was relatively stationary and corresponded to the higher end (10–13  $\mu\text{m}$   $Ra$ ). An examination of the side surfaces to decipher this behaviour showed a conspicuous presence of bonded metal particles that are either only partially melted or unmelted (Fig. 4), the incidence of which appears to have had a dominating influence on the surface roughness. The exposure of powder particles adjacent to the edges to thermal energy insufficient for complete melting combined with short solidification time could result in their formation [18]. Such features did not but influence the CA measurements, with values being on the same order ( $80^\circ$ – $100^\circ$ ) as those on the top surfaces; for instance, Fig. 3b

shows droplet geometry for either end of roughness with CA of  $85^\circ$  and  $92^\circ$ . Notwithstanding the fact that the CA of as-built surfaces was not markedly influenced by these globular microstructures, considering their resemblance to hierarchical features (albeit of a larger scale) on biological surfaces such as lotus leaves that significantly promote hydrophobicity [19], their role will be revisited later in this paper in the context of textured surfaces.

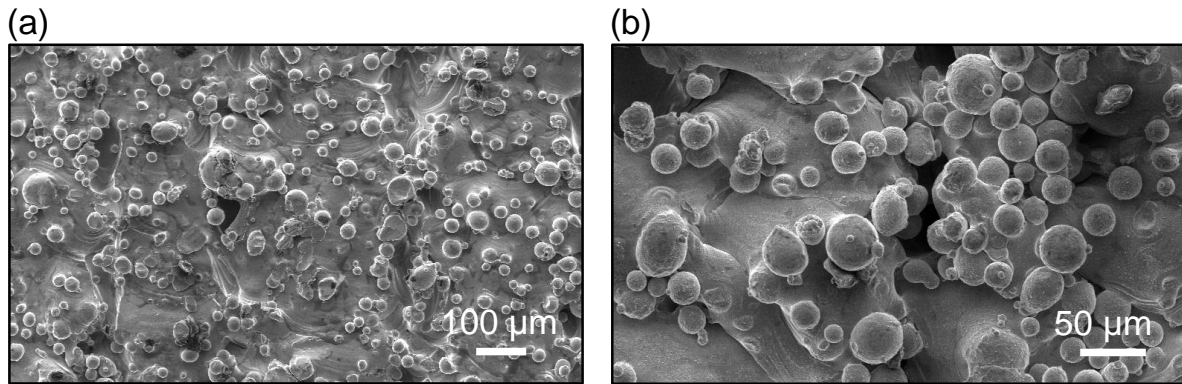


Fig. 4. Topography of side surfaces at two length scales.

### 3.2. Assessment of limiting feature geometry

This subsection presents results obtained from printing the four artifacts (Sec.2.2) designed to gather information on the limiting feature geometry. The first artifact (Fig. 1a) focused on the evaluation of the minimum width for protruding and sunk features by printing trapezoids. The trapezoid sides changed linearly from 0.01 mm to 0.60 mm over a length of 45 mm. Fig. 5a depicts a region on this artifact which shows the limiting feature width at two magnifications for protruding features. The trapezoids were not adequately deposited at an approximate distance of 5 mm along the coupon length from the smaller parallel side of the trapezoid (0.01 mm). This corresponds to a minimum width of 0.09 mm by design, however, the width at this location was measured to be 0.13 mm, which may be reconciled in terms of the effective spot size of the laser and the programmed beam offset. Fig. 5a further makes it evident that the minimum width is largely independent of the feature height over the range investigated (one to twelve layer thickness of 0.04 mm each).

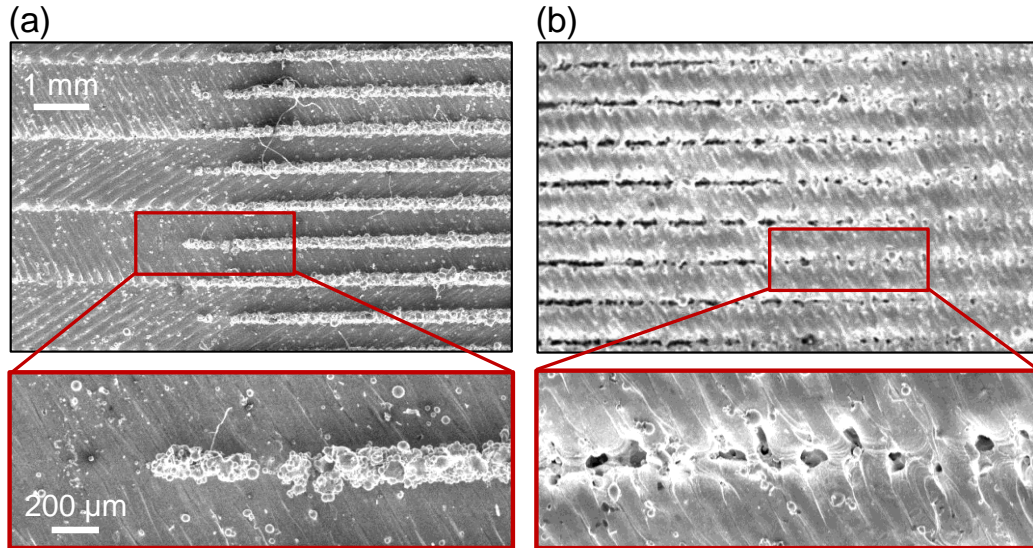


Fig. 5. Minimum width for: (a) protruding, and (b) sunk features.

Relative to the protruding features above, locations at which the sunken trapezoids were not adequately resolved entailed a larger variation (Fig. 5b). Well defined open channels could be observed at a distance of  $\sim 10$  mm from the edge, which corresponds to a width of 0.14 mm as per the design. In line with the protruding features, the actual width at this location was somewhat lower and was measured to be 0.10 mm, on account of the material closing in on the sunk features. Characterization of the first artifact thus indicated the limiting feature widths to be 0.13 mm and 0.10 mm for protruding and sunk features, respectively.

Fig. 6a and 6b portray printed versions of the second artifact that was designed (Fig. 1b) to assess the minimum spacing between protruding and sunk features. The minimum spacing controls such indices as the feature density and area fraction that have been found to be decisive in tribological [20, 21] and surface wetting [19] applications. For a fixed protruding feature width of 0.4 mm, the minimum achievable spacing was measured to be 0.11 mm, which was lower than the design spacing of 0.15 mm (Fig. 6a), as expected. Likewise, the corresponding spacing for sunk features (Fig. 6b) was measured to be 0.13 mm, which is higher than the design value (0.09 mm). It is interesting to note that the minimum spacing values (0.13 and 0.09 mm) are similar to the corresponding minimum feature widths (Fig. 5).

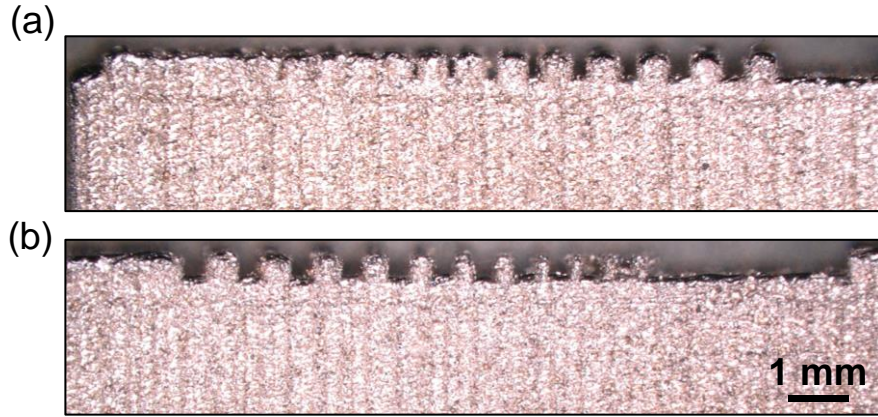


Fig. 6. Minimum spacing for: (a) protruding, and (b) sunk features.

For both artifacts discussed above, the measured minimum feature dimensions were independent of the SLM process parameters employed with reference to the maximum strength and density (Table 1). To further expand on the process parameter domain, single tracks were printed over a wide range of laser power (50–370 W) and scanning speeds (200–2000 mm/s), and the width of such tracks was measured at different locations along the track. Fig. 7 shows the average track width, with the effects of the laser power and scanning speed consolidated in terms of the linear energy density  $E_L$ . The figure shows the track width distribution to be rather skewed between 0.1 mm and 0.15 mm. This is quite in alignment with the findings of feature dimensions obtained from the three artifacts already discussed. Examination of the fabricated tracks indicated noticeable balling at a low energy density (Fig. 8a), this phenomenon is but not quite suitable to print robust structured surfaces due to its inherent randomness. Fig. 8b and 8c show tracks that correspond to the lower (0.1 mm) and higher (0.2 mm) ends of track width. Fig. 8d underscores the utilization of an appropriate combination of laser power and scanning speed towards obtaining consistent tracks under stable melting, which is an additional consideration along with the minimum width, for robust texturing.

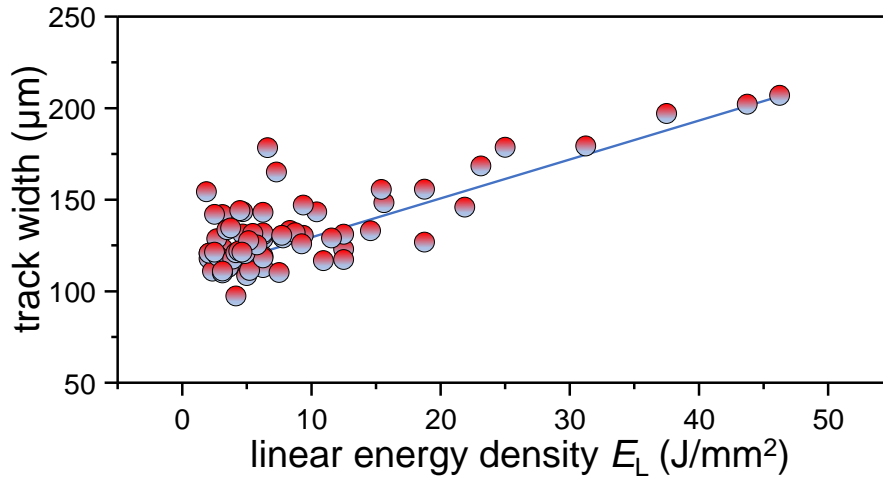


Fig. 7. Single track width as a function of linear energy density.

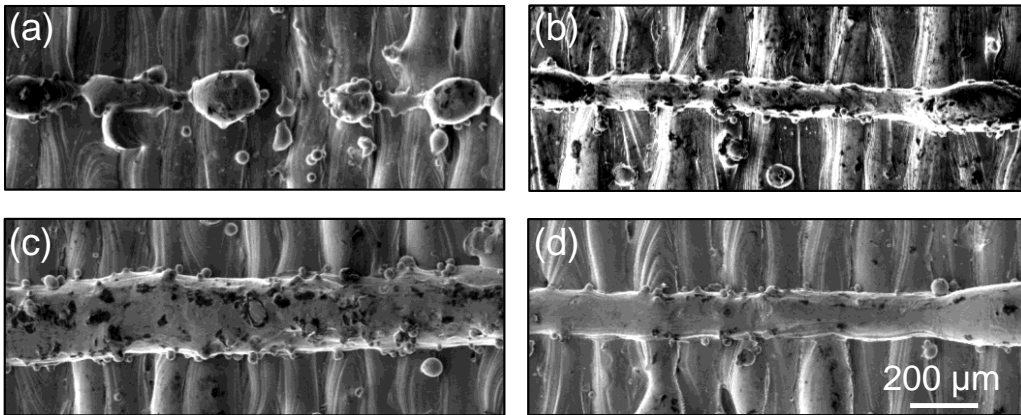


Fig. 8. Single tracks obtained under different combinations of laser power and scanning speed: (a) 50 W, 400 mm/s, (b) 200 W, 1200 mm/s, (c) 370 W, 200 mm/s, and (d) 300 W, 800 mm/s.

### 3.3. Contact angle of additively textured surfaces

With a focus on controlling surface wettability, additively textured patterns were investigated on both the top and side surfaces, as indicated in Sec. 3.2. The top surface entailed square pillars and rectangular channels, and the side surface involved re-entrant and rectangular channels (Fig. 2). The dimensions of these textured features (Table 2) were set on the basis of the knowledge obtained from building and characterizing artifacts that were designed to inform limiting feature sizes (Fig. 1).

On the top surface, the first pattern referred to an array of square pillars with side lengths of 0.10 mm and 0.15 mm, over a range of spacing (0.15–0.25 mm) and height (0.04–0.16 mm). Fig. 9a and 9b show pillars with side lengths of 0.10 mm and 0.15 mm, respectively; they were of the same spacing (0.25 mm) and height (0.12 mm). The pillars can be seen to comprise largely circular sections and rounded tops, rather than the intended square cross-sections and flat tops, owing to surface tension effects. For a pillar side length of 0.1 mm, the pattern array can be observed to be fairly irregular with several evident instances of local build failures (Fig. 9a). The occurrence of such could be reduced significantly by increasing the pillar side length to 0.15 mm (Fig. 9b). Fig. 9 further shows the corresponding droplet shapes that indicate the respective CA to be  $137^\circ$  and  $125^\circ$ , which is a significant increase over that of as-built surfaces that were on the order of  $80^\circ$ – $100^\circ$  (Fig. 3). It is further interesting to note that the obtained CA are comparable to those measured on pillar arrays of a similar geometry that were micro-milled from polymethyl methacrylate [22].

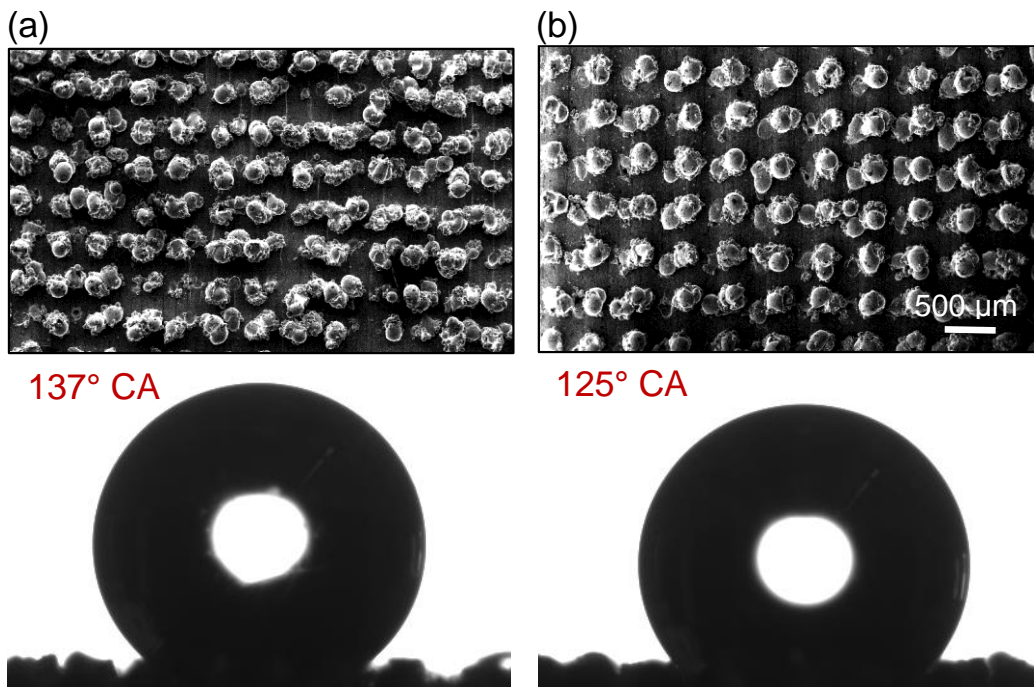


Fig. 9. Pillar array surfaces with side lengths of: (a) 0.1 mm, and (b) 0.15 mm, and the associated droplets.

Wetting of rough surfaces has classically been viewed in terms of models due to Wenzel and Cassie-Baxter [12, 23]. The Wenzel model describes the homogenous wetting regime wherein the fluid intrudes into the surface interstices, with the apparent or static CA of a rough surface

$\Theta_w$  related to the Young or equilibrium contact angle  $\Theta$  of an ideal surface as:  $\cos \Theta_w = r \cos \Theta$ , where the roughness factor  $r$  is the ratio of the actual and projected surface areas. The Cassie-Baxter model extends the concept further to partial wetting of heterogeneous surfaces such as feathers and lotus leaves, wherein the surface is deemed to be a composite solid-liquid-air interface, with surface troughs constituting air pockets that support droplets on surface peaks. The corresponding static contact angle  $\Theta_{CB}$  is obtained as  $[f \cos \Theta + (f-1)]$  where  $f$  is the solid area fraction. For a pillar array,  $f$  can be calculated [22] as  $[p^2/(p+c)^2]$ , where the parameters  $p$  and  $c$  are the pillar side length and spacing, respectively (Fig. 2a).

The decrease in CA from  $137^\circ$  to  $125^\circ$  with an increase in pillar side length from 0.10 mm to 0.15 at a constant spacing (Fig. 9) is in qualitative agreement with the Cassie-Baxter model above. Likewise, the CA should exhibit an increase with higher spacing parameter  $c$ , which was consistent with measurements (Fig. 10a). The CA did exhibit a relatively significant change (Fig. 10b) with the pillar height over the range investigated (one to four layers: 0.04 to 0.16 mm). The higher CA associated with the pillars of a height spanning three and four layers may be attributed to the transition of the water droplets from the Wenzel to the Cassie-Baxter state. Such a transition occurs when the maximum droop of the water droplet  $[2c^2/(8R)]$  between pillars (where  $R$  is the water drop radius) is more than the pillar height [24].

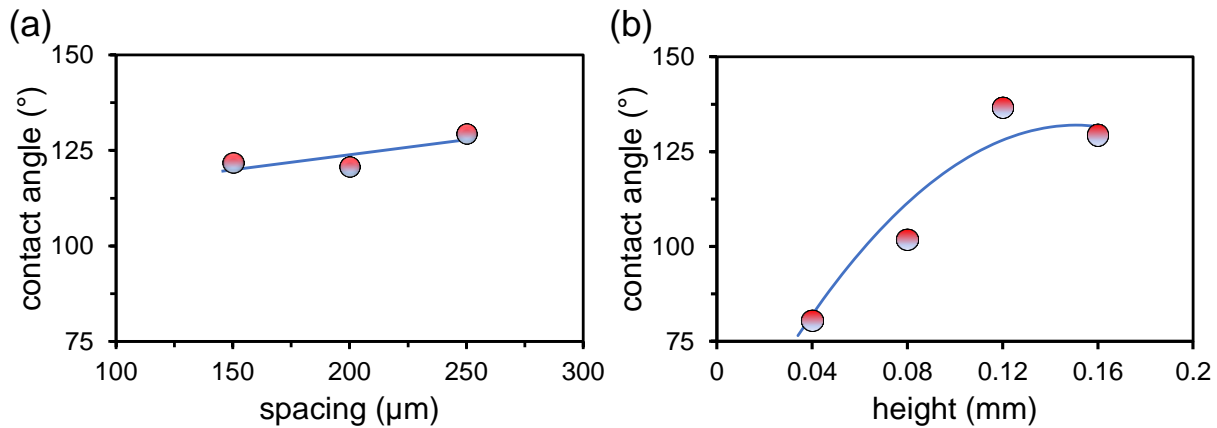


Fig. 10. CA for 0.1 mm side length pillars at: (a) 0.16 mm pillar height, and (b) 0.25 mm pillar spacing.

The second texturing pattern on the top surface referred to rectangular channels spanning a range of pitch (0.2–0.5 mm) and height (0.04–0.20 mm). The channels were built by using higher values for the hatch spacing resulting in separated singletracks, with a variable width associated

with the process parameters (Fig. 7). Fig. 11a and 11b show two channels with a pitch of 0.2 mm and 0.5 mm, and a height of 0.2 mm. The channel features were consistently of better quality, with no local build failures as in the case of micropillars (Fig. 9). Fig. 11 further shows the corresponding droplet shapes, which indicate the CA to have increased significantly from  $97^\circ$  to  $136^\circ$  for an increase in spacing by a factor of 2.5. Fig. 12a presents data showing an increase in CA with hatch spacing, at a fixed height of 0.2 mm. Such an increase is in qualitative agreement with the Cassie-Baxter model, and may be attributed to the change in solid area fraction, which is calculated [22] for channels as  $[w/h]$ , where  $w$  is the track width and  $h$  is the hatch spacing. The average track width associated with 800 m/s scanning speed and 300 W power was approximately 0.14 mm (Fig. 8d).

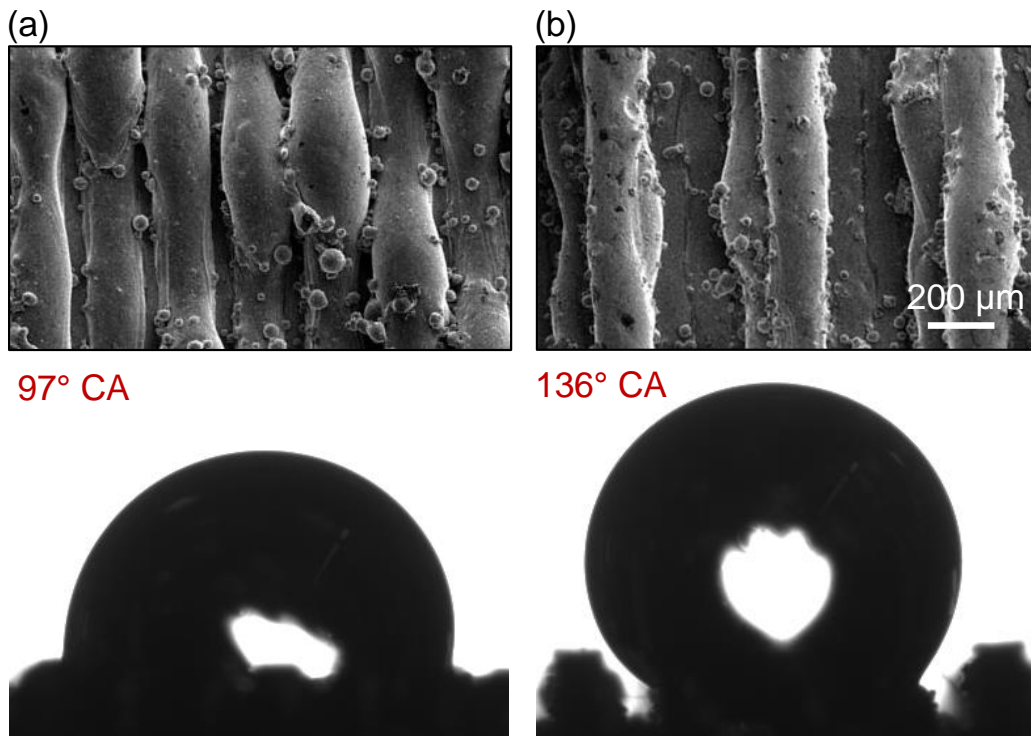


Fig. 11. Channels patterns and the associated CA for spacing: (a)  $h = 0.2$  mm (b)  $h = 0.5$  mm.

Fig. 12b shows the CA to also generally increase with channel height (number of layers). Over the investigated range, the pitch can be observed to have a greater impact on the CA compared to the height. CA shown in Fig. 12a and 12b are comparable to those measured on channel arrays of similar geometry, micro-milled from polymethyl methacrylate [22]. Further investigations indicated channel patterns to exhibit wetting anisotropy, with CA values measured parallel to the

channel length corresponding to a decrease of  $10^\circ$  to  $15^\circ$  relative to those measured across. This signifies a relative elongation of the droplet along the channel length, similar to that reported in the case of steel microchannels machined using wire EDM [25].

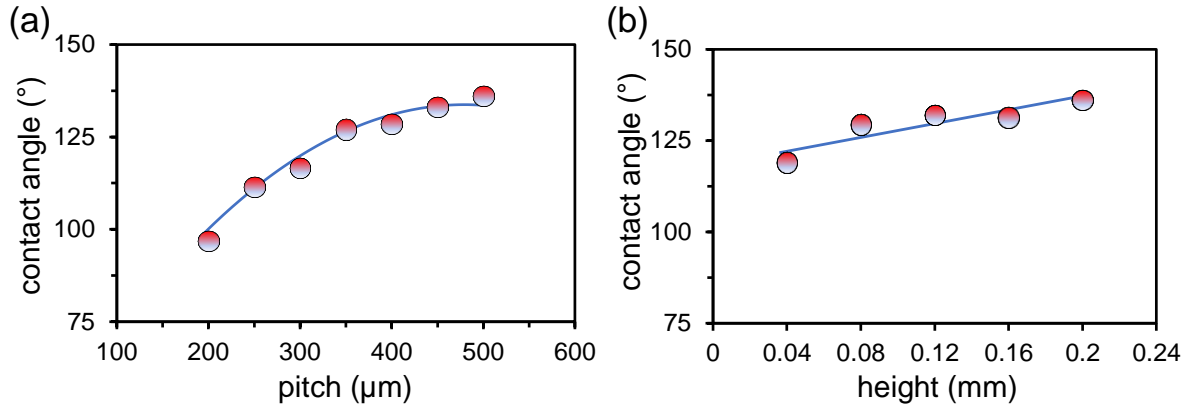


Fig. 12. CA for channels array at: (a) 0.2 mm height (b) 0.5 mm pitch.

The mushroom-like geometry of re-entrant channels comprises air pockets that support water droplets in the composite solid-liquid-air state, preventing them from intruding into the relief structures in between. This geometry increases the energy threshold at which the transition from Cassie-Baxter to Wenzel states occurs [26], thereby promoting hydrophobicity even in materials that are inherently hydrophilic [26], and for liquids with a surface tension lower than that of water [27]. Such structures machined using micro-wire EDM have for instance been shown to exhibit superhydrophobicity in [28]. Additive manufacturing of overhanging structures on the top surface (perpendicular to the build direction) in general necessitates gradual inclinations [29] or support structures, the provision of which is but not realistic in the current context that involves re-entrant features on the microscale. This issue was circumvented in the present work by realizing the re-entrant channels on the side surface parallel to the build direction as shown in Fig. 2c, in which case there are no overhanging features. Fig. 13 presents a proof of concept of this approach. The distortion in the printed structure relative to the intended design (Fig. 2c), appears to arise from the large height (7 mm) of the features along the print direction relative to the re-entrant feature dimensions ( $p = 100 \mu\text{m}$  and  $c = 200 \mu\text{m}$ ). This notwithstanding, the corresponding CA was  $126^\circ$  (Fig. 13), which is a significant increase over those of as-built side surfaces that exhibited values ranging between  $80^\circ$  and  $100^\circ$  (Fig. 3).

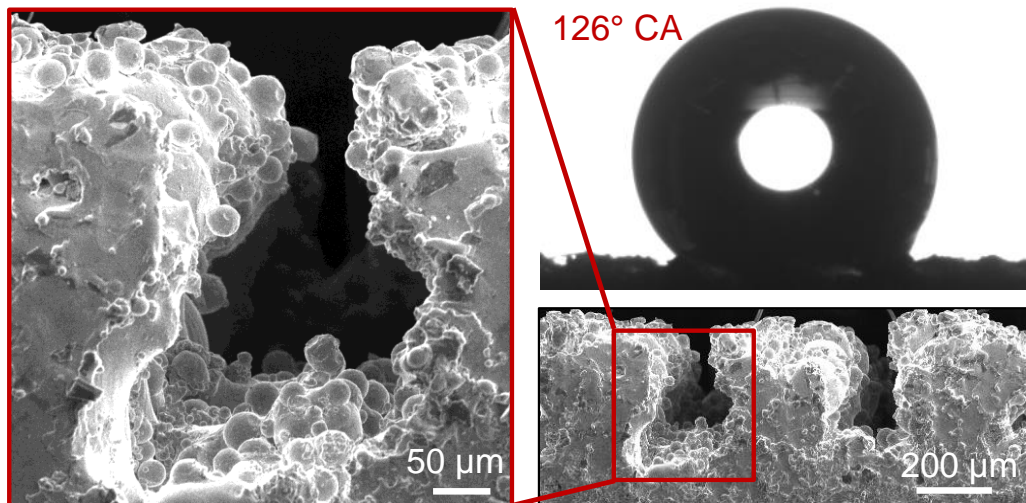


Fig. 13. Re-entrant structures on the side surface and the associated droplet shape.

The transition from Cassie-Baxter to Wenzel states is influenced by multiple destabilizing factors such as capillary waves, droplet condensation, surface inhomogeneities and liquid pressure. Given the scale dependency of these factors, a hierarchical texture is beneficial to realize a stable Cassie-Baxter state [19]. Partially melted metal powder particles of an approximate size of 0.03 mm adhering to the sidewalls (Fig. 4), which are smaller than the limiting feature dimensions of the texture, could constitute such a desired hierarchical secondary texture on top of the primary channel features and enhance the CA. To test this hypothesis, channels ( $p = 100 \mu\text{m}$  and  $c = 250 \mu\text{m}$ ) were fabricated on the side surface as shown in Fig. 2d.

Fig. 14 shows the primary channels as well as the secondary texture signifying their hierarchical nature, which resulted in a CA of  $141^\circ$  (Fig. 14). It may be noted that the partially melted powder particles on the sidewall channels (Fig. 14) are similar to those on the as-built side surfaces (Fig. 4). While the side as-built surfaces comprising partially melted powder corresponded to contact angles of just around  $90^\circ$  (Fig. 3b), such a topography when overlaid on a primary texture comprising channels yielded a contact angle of  $141^\circ$  (Fig. 15b). This implies that the mechanism behind the enhancement of hydrophobicity is indeed the hierarchical nature of the printed surface. Given the inadequacy of easy-to-measure but too simplistic a roughness parameter as  $Ra$  to capture the intricacies of a phenomenon as complex as wetting (Fig. 3) and the highlighted importance of a hierarchical structure in the context of wettability (Fig. 15), it is appropriate and

essential to apply multi-scale surface analyses [30] to gain additional insights into the underlying mechanisms.

Fig. 15 shows a comparison of the topography of channels with similar dimensions on the top (Fig. 15a) and side surfaces (Fig. 15b); the increase in CA from  $132^\circ$  to  $141^\circ$  proves the hypothesis that the increase in CA can be attributed to the secondary structure pertaining to the adhered partially molten particles. Should a component necessitate it, hierarchical top surfaces may be printed by spreading metal powder of a size consistent with the application, and then tailoring the laser power intensity to fuse the particles into the built surface as opposed to melting them completely. The highest CA of  $141^\circ$  obtained in this work being significantly higher than that of as-built AM surfaces ( $80^\circ$  to  $100^\circ$ ), validates the notion of additive texturing proposed in this paper, in the context of controlled surface wetting.

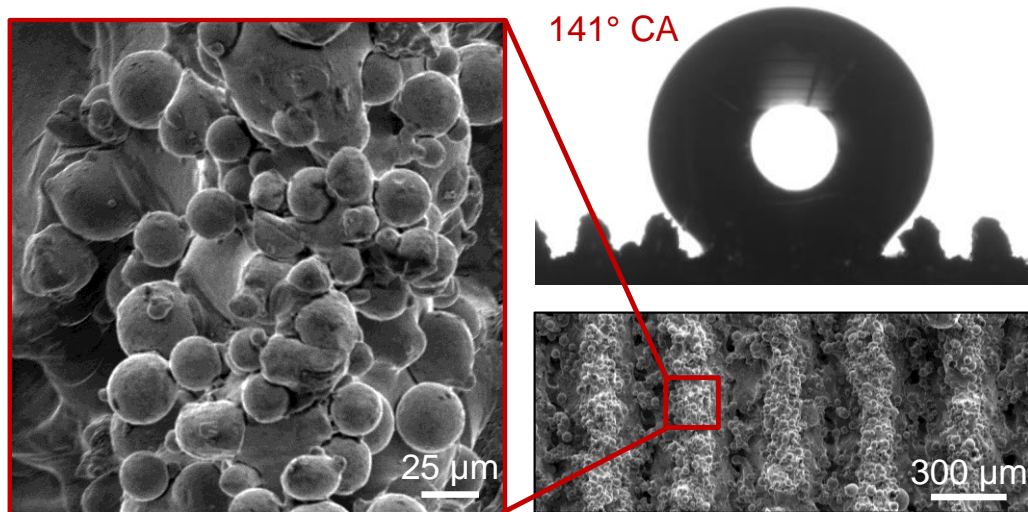


Fig. 14. Channels on the side surface and the corresponding droplet shape.

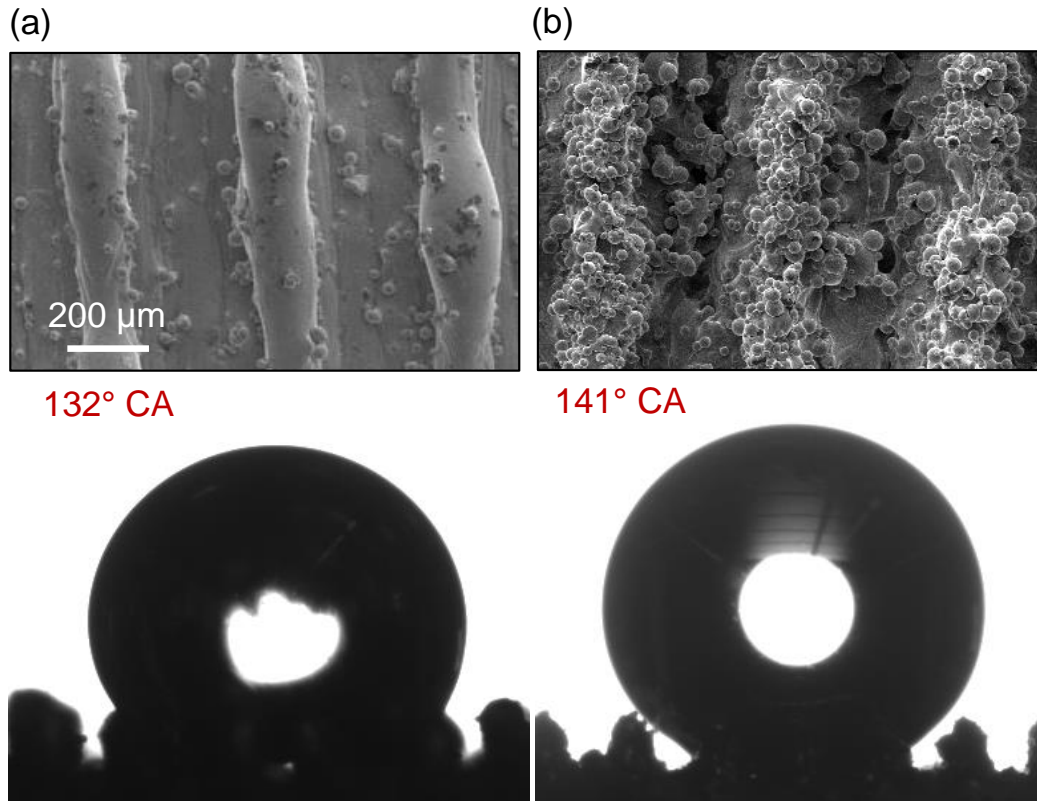


Fig. 15. Comparison of channels with equivalent dimensions on: (a) top, and (b) side surfaces.

## 4. Conclusions

Intending to extend the functionality of AM components, this research presented Additive Texturing as an innovative approach for the in-process fabrication of metallic hydrophobic surfaces, with no need for additional post-processing operations. The work led to the following conclusions:

- The volumetric energy density showed a significant influence on the roughness of top surfaces in SLM. A five-fold change in roughness in terms of the  $Ra$  parameter but corresponded to only a minimal variation ( $80^{\circ}$ – $100^{\circ}$ ) in the water CA.
- Due to partially melted powder particles adhering to the side surface, the influence of process parameters on both the surface roughness and wettability was minimal.
- Investigations indicated SLM with a continuous laser to correspond to a minimum feature width of 100–150  $\mu\text{m}$ , which is equivalent to the single track width.

- For texture dimensions consistent with the limiting width, channel arrays were more reproducible and defect-free compared to pillar arrays and re-entrant channel patterns. Printing of the patterns above on the top surface indicated the channel patterns to also correspond to the highest CA of  $\sim 136^\circ$ .
- Realizing channel patterns on the side surface further enhanced the CA by about  $10^\circ$  on account of the hierarchical dual-scale structure arising from the adherence of partially molten metal powder.
- Additively textured surfaces corresponded to a CA of up to  $141^\circ$  which is a significant increase over the range ( $80^\circ$ – $100^\circ$ ) exhibited by as-built surfaces.

This research focussed on surface wetting as an avenue to introducing the concept of Additive Texturing. The results obtained point to the significant capacity of this novel concept for likewise tailoring AM for printing functional surfaces, towards further enhancing its process capability and application potential.

## Acknowledgment

This work was funded in part by the Natural Sciences and Engineering Research Council (NSERC) of Canada.

## References

- [1] T. DebRoy, H. Wei, J. Zuback, T. Mukherjee, J. Elmer, J. Milewski, A.M. Beese, A. Wilson-Heid, A. De, W. Zhang, [Additive manufacturing of metallic components—process, structure and properties](#), Progress in Materials Science 92 (2018) 112–224.
- [2] J.Y. Ho, K.K. Wong, K.C. Leong, [Saturated pool boiling of FC-72 from enhanced surfaces produced by selective laser melting](#), International Journal of Heat and Mass Transfer 99 (2016) 107–121.
- [3] A. Townsend, N. Senin, L. Blunt, R. Leach, J. Taylor, [Surface texture metrology for metal additive manufacturing: A review](#), Precision Engineering 46 (2016) 34–47.
- [4] A.P. Malshe, S. Bapat, K.P. Rajurkar, H. Haitjema, [Bio-inspired textures for functional applications](#), CIRP Annals 67(2) (2018) 627–650.
- [5] Q. Ma, Z. Tong, W. Wang, G. Dong, [Fabricating robust and repairable superhydrophobic surface on carbon steel by nanosecond laser texturing for corrosion protection](#), Applied Surface Science 455 (2018) 748–757.
- [6] C. Guo, P. Koshy, F. Coelho, P.R. Selvaganapathy, [Sink electrical discharge machining of hydrophobic surfaces](#), CIRP Annals 68(1) (2019) 185–188.

- [7] J.A. Wahab, M.J. Ghazali, W.M.W. Yusoff, Z. Sajuri, [Enhancing material performance through laser surface texturing: a review](#), Transactions of the IMF 94(4) (2016) 193–198.
- [8] L. Rebaioli, I. Fassi, [A review on benchmark artifacts for evaluating the geometrical performance of additive manufacturing processes](#), The International Journal of Advanced Manufacturing Technology 93(5–8) (2017) 2571–2598.
- [9] S. Moylan, J. Slotwinski, A. Cooke, K. Jurens, M.A. Donmez, [An additive manufacturing test artifact](#), Journal of Research of the National Institute of Standards and Technology 119 (2014) 429.
- [10] M.K. Thompson, M. Mischkot, [Design of test parts to characterize micro additive manufacturing processes](#), Procedia CIRP 34 (2015) 223–228.
- [11] M. Yakout, M.A. Elbestawi, S.C. Veldhuis, [Density and mechanical properties in selective laser melting of Invar 36 and stainless steel 316L](#), Journal of Materials Processing Technology 266 (2019) 397–420.
- [12] K.-Y. Law, H. Zhao, [Surface wetting: Characterization, contact angle, and fundamentals](#), Springer, Switzerland, 2016.
- [13] Z.N. Xu, [An algorithm for selecting the most accurate protocol for contact angle measurement by drop shape analysis](#), Review of Scientific Instruments 85(12) (2014) 125107.
- [14] D. Wang, Y. Liu, Y. Yang, D. Xiao, [Theoretical and experimental study on surface roughness of 316L stainless steel metal parts obtained through selective laser melting](#), Rapid Prototyping Journal (2016).
- [15] S.J. Foster, K. Carver, R.B. Dinwiddie, F. List, K.A. Unocic, A. Chaudhary, S.S. Babu, [Process-defect-structure-property correlations during laser powder bed fusion of alloy 718: Role of in situ and ex situ characterizations](#), Metallurgical and Materials Transactions A 49(11) (2018) 5775–5798.
- [16] D. Kam, S. Bhattacharya, J. Mazumder, [Control of the wetting properties of an AISI 316L stainless steel surface by femtosecond laser-induced surface modification](#), Journal of micromechanics and microengineering 22(10) (2012) 105019.
- [17] J. Long, M. Zhong, H. Zhang, P. Fan, [Superhydrophilicity to superhydrophobicity transition of picosecond laser microstructured aluminum in ambient air](#), Journal of Colloid and Interface Science 441 (2015) 1–9.
- [18] T. Yang, T. Liu, W. Liao, E. MacDonald, H. Wei, X. Chen, L. Jiang, [The influence of process parameters on vertical surface roughness of the AlSi10Mg parts fabricated by selective laser melting](#), Journal of Materials Processing Technology 266 (2019) 26–36.
- [19] B. Bhushan, Y.C. Jung, [Natural and biomimetic artificial surfaces for superhydrophobicity, self-cleaning, low adhesion, and drag reduction](#), Progress in Materials Science 56(1) (2011) 1–108.
- [20] T. Ibatan, M.S. Uddin, M.A.K. Chowdhury, [Recent development on surface texturing in enhancing tribological performance of bearing sliders](#), Surface and Coatings Technology 272 (2015) 102–120.
- [21] A.F.S. Baharin, M.J. Ghazali, J.A. Wahab, [Laser surface texturing and its contribution to friction and wear reduction: A brief review](#), Industrial Lubrication and Tribology (2016).
- [22] Z. Shi, X. Zhang, [Contact angle hysteresis analysis on superhydrophobic surface based on the design of channel and pillar models](#), Materials & Design 131 (2017) 323–333.
- [23] M.A. Nilsson, R.J. Daniello, J.P. Rothstein, [A novel and inexpensive technique for creating superhydrophobic surfaces using Teflon and sandpaper](#), Journal of Physics D: Applied Physics 43(4) (2010) 045301.

- [24] Y.C. Jung, B. Bhushan, [Wetting transition of water droplets on superhydrophobic patterned surfaces](#), *Scripta Materialia* 57(12) (2007) 1057–1060.
- [25] W.-G. Bae, D. Kim, K.Y. Song, H.E. Jeong, C.N. Chu, [Engineering stainless steel surface via wire electrical discharge machining for controlling the wettability](#), *Surface and Coatings Technology* 275 (2015) 316–323.
- [26] G. Whyman, E. Bormashenko, [How to make the Cassie wetting state stable?](#), *Langmuir* 27(13) (2011) 8171–8176.
- [27] R. Dufour, G. Perry, M. Harnois, Y. Coffinier, V. Thomy, V. Senez, R. Boukherroub, [From micro to nano reentrant structures: hysteresis on superomniphobic surfaces](#), *Colloid and Polymer Science* 291(2) (2013) 409–415.
- [28] P.B. Weisensee, E.J. Torrealba, M. Raleigh, A.M. Jacobi, W.P. King, [Hydrophobic and oleophobic re-entrant steel microstructures fabricated using micro electrical discharge machining](#), *Journal of Micromechanics and Microengineering* 24(9) (2014) 095020.
- [29] D. Wang, S. Mai, D. Xiao, Y. Yang, [Surface quality of the curved overhanging structure manufactured from 316-L stainless steel by SLM](#), *The International Journal of Advanced Manufacturing Technology* 86(1) (2016) 781–792.
- [30] C.A. Brown, H.N. Hansen, X.J. Jiang, F. Blateyron, J. Berglund, N. Senin, T. Bartkowiak, B. Dixon, G. Le Goïc, Y. Quinsat, W.J. Stemp, M.K. Thompson, P.S. Ungar, E.H. Zahouani, [Multiscale analyses and characterizations of surface topographies](#), *CIRP Annals* 67(2) (2018) 839–862.